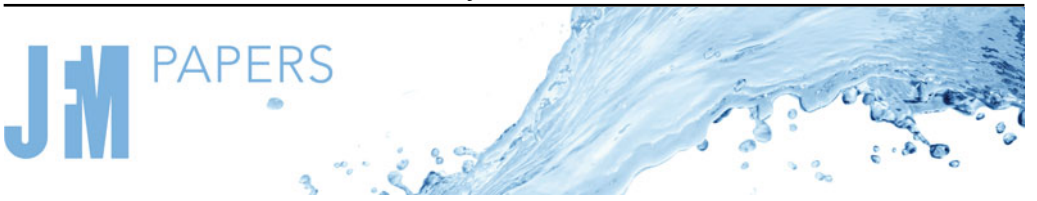
J. Fluid Mech. (2026), *vol.* 1030, A65, doi:10.1017/jfm.2026.11309



Direct numerical simulations of channel flow with a molecular-dynamics-informed wall slip boundary condition

Abdul Aziz Shuvo[1], **Bladimir Ramos Alvarado**[1] **and Xiang I.A. Yang**[1]

[1]Mechanical Engineering, The Pennsylvania State University, University Park, PA 16802, USA

Corresponding authors: Xiang I.A. Yang, xzy48@psu.edu; Bladimir Ramos Alvarado, bzr52@psu.edu

(Received 18 August 2025; revised 13 February 2026; accepted 16 February 2026)

Recent molecular-level simulations suggest that slip at solid–liquid interfaces can depend on shear. This work integrates molecular dynamics (MD) and direct numerical simulations (DNS) to quantify how shear-dependent slip modifies near-wall turbulence in wall-bounded flows. The MD is used to characterise how the slip length depends on wall shear stress across a range of solid–liquid affinities, revealing a threshold-like, bimodal response: the slip length is approximately constant at low and high stresses, with a sharp transition near a slip-activation threshold. This MD-derived relation is then implemented as a wall boundary condition in DNS of turbulent channel flow at friction Reynolds numbers 180, 400 and 1000, using five threshold values to represent different interfacial affinities. The DNS show that the logarithmic region is largely preserved, aside from an approximately constant upward shift, while the near-wall turbulence is modified through changes in the streamwise Reynolds stress. In particular, the streamwise turbulence intensity in the viscous sublayer is strongest when the mean wall stress is close to the slip-activation threshold, and it weakens as the mean stress moves away from that threshold. Analysis further indicates that shear-dependent slip reduces near-wall dissipation and promotes elongated near-wall coherent structures. Finally, a mean flow model that incorporates shear-dependent slip shows good agreement with the DNS mean velocity profiles. Overall, this work provides a multiscale framework that links molecular interfacial physics to continuum-scale turbulence.

Key words: turbulence modelling, turbulence simulation, molecular dynamics

© The Author(s), 2026. Published by Cambridge University Press. This is an Open Access article, distributed under the terms of the Creative Commons Attribution licence (https://creativecommons.org/licenses/by/4.0/), which permits unrestricted re-use, distribution and reproduction, provided the original article is properly cited.

https://doi.org/10.1017/jfm.2026.11309 Published online by Cambridge University Press

1. Introduction

When there is slip in the streamwise direction at the wall, the boundary condition becomes

$$u - L_s \frac{\partial u}{\partial z} = 0, \tag{1.1}$$

where u is the streamwise velocity, L_s is the slip length, and z is the wall-normal direction. The effect of wall slip on turbulent drag has been studied extensively. Min & Kim (2004) performed direct numerical simulations (DNS) of fully developed turbulent channel flow at $Re_\tau = 180$ with Navier-slip boundary conditions. With streamwise slip only, they reported substantial drag reduction that increased with slip length, reaching approximately 29 % at $L_s^+ = 3.566$; with spanwise slip only, they observed drag increase accompanied by strengthened near-wall activity. Consistent with this, Busse & Sandham (2012) showed that anisotropic slip can substantially alter drag: streamwise slip promotes drag reduction, whereas spanwise slip tends to increase drag, and they identified a threshold streamwise slip length beyond which drag is reduced irrespective of the spanwise slip. Park, Park & Kim (2013) emphasised that drag reduction correlates strongly with an effective slip length: the normalised drag decreases rapidly as the effective slip increases up to $\lambda^+ \approx 30$–40, after which it varies only weakly with further increases in slip. Yoon *et al.* (2016) reported that slip conditions elongate near-wall coherent structures, and at bulk Reynolds number 10 333, yielded approximately a 35 % reduction in skin friction; they further estimated that large-scale structures and their near-wall imprints contribute a substantial fraction of this reduction. Finally, Ibrahim *et al.* (2021) proposed a unifying virtual-origin framework for turbulence over drag-altering surfaces under Robin-type constant-slip boundary conditions. A key element is the distinction between the apparent origin perceived by the mean flow, ℓ_U, and that perceived by the turbulence, ℓ_T. By imposing slip in Fourier space, they showed that the streamwise slip applied to the mean mode ($k = 0$) and to the fluctuating modes ($k \neq 0$) can be prescribed independently (i.e. $\ell_{x,m}$ versus $\ell_{x,f}$), enabling separate control of the mean flow shift and near-wall streamwise intensity within a time-invariant constant-slip setting. They also showed that ℓ_T is governed primarily by the cross-flow wall conditions (wall-normal and spanwise components), and that aligning the virtual origins leads to the collapse of turbulence statistics towards smooth-wall-like behaviour in appropriately shifted/scaled coordinates.

Previous computational studies, including the ones cited above, have often modelled hydrodynamic slip as a constant parameter in the slip boundary condition. This is an oversimplification, as hydrodynamic slip is an interfacial phenomenon governed by complex interactions at the solid–liquid interface and the local wall shear stress (Thompson & Troian 1997; Martini *et al.* 2008*a*; Kannam *et al.* 2011; Ramos-Alvarado, Kumar & Peterson 2016; Wagemann *et al.* 2017; Shuvo *et al.* 2025). Experimental investigations provide evidence that L_s is shear-dependent. Craig, Neto & Williams (2001) measured hydrodynamic drainage forces in a Newtonian fluid using an atomic force microscope. Their results showed that L_s increased linearly with shear rate. Choi, Westin & Breuer (2003) conducted experiments on water flow in microchannels, and observed a comparable linear relationship between L_s and shear rate. Further investigations by Li, Mo & Li (2014) revealed that L_s increases linearly with shear rate once a critical shear rate is exceeded. At high shear rates, L_s asymptotes to a constant value. This transition highlights the dual influence of solid–liquid affinity and shear rate on the development of hydrodynamic slip. While experimental techniques have advanced significantly, their resolution remains limited in capturing the full complexity of interfacial interactions. Consequently, molecular dynamics (MD) simulations have been increasingly employed to investigate atomic-scale mechanisms governing hydrodynamic

https://doi.org/10.1017/jfm.2026.11309 Published online by Cambridge University Press

slip. The behaviour of L_s varies significantly under different shear conditions, with reports of both bounded and unbounded growth at high shear rates. Thompson & Troian (1997) performed non-equilibrium MD (NEMD) simulations of shear-driven flow, and observed that L_s remained constant at low shear rates but exhibited rapid growth beyond a critical shear rate. Similar trends were reported in shear-driven MD simulations by Voronov, Papavassiliou & Lee (2006, 2007) and Chen *et al.* (2006), where L_s increased sharply after exceeding a critical shear threshold. Conversely, Martini *et al.* (2008*a*) argued that the unbounded growth of L_s at high shear rates was an artefact of rigid wall models that neglect solid–liquid momentum exchange. Using NEMD simulations of Couette flow, they showed that while rigid walls yield unbounded L_s, flexible walls accounting for atomic vibrations and viscous dissipation produce bounded L_s. Furthermore, other studies have reported a reduction in L_s at high shear rates (Alizadeh Pahlavan & Freund 2011; Ramos-Alvarado *et al.* 2016). Alizadeh Pahlavan & Freund (2011) attributed this reduction to local viscous heating caused by an increase in solid–liquid collisions. These contrasting findings suggest that the dependence of L_s on shear rate and interfacial properties remains unclear.

Despite extensive molecular-scale insights, few continuum-scale models have incorporated shear-dependent slip boundary conditions derived from MD simulations. In the present work, we performed NEMD simulations of shear-driven flow to characterise the behaviour of L_s under different solid–liquid interactions, ranging from hydrophilic to hydrophobic conditions. Based on these findings, we formulated a shear- and interaction-dependent L_s model, and incorporated it into DNS of turbulent channel flows. The DNS framework enables us to investigate the impact of this molecular-level-informed slip boundary condition on near-wall turbulence structures and statistics. In addition, we developed a model for the mean momentum balance incorporating shear-dependent L_s, aiming to predict velocity profiles and near-wall turbulence intensity. This multiscale approach offers a physically grounded framework that links molecular interfacial behaviour with continuum turbulence modelling, enabling a deeper understanding of slip effects in wall-bounded turbulent flows.

2. Computational details

2.1. *The MD simulation set-up*

The MD simulations provide a molecular-level framework capable of resolving interfacial phenomena beyond the continuum approximation of the Navier–Stokes equations (Thompson & Troian 1997; Martini *et al.* 2008*a*; Alizadeh Pahlavan & Freund 2011; Ramos-Alvarado *et al.* 2016; Shuvo *et al.* 2024*a*, 2025). They solve Newton's second law of motion ($F = ma$), where F represents the force acting on an atom, m is the atomic mass, and a is its acceleration. In MD simulations, F is calculated using an empirical force field, which defines the potential energy landscape as a function of the relative distance between atoms (Rapaport 2004; Frenkel & Smit 2023). This classical framework captures the essential physics of bonded and non-bonded interactions, thereby facilitating the calculation of L_s as a function of interfacial properties and operating conditions.

In our MD simulations, we investigated shear-driven water flow confined between two parallel graphite walls to elucidate the influence of solid–liquid affinity on L_s; see figure 1(*a*). The MD simulations were conducted using the large-scale atomic/molecular massively parallel simulator (LAMMPS) (Plimpton 1995), and the atomic trajectories were visualised using OVITO (Stukowski 2009). To model shear-driven flow, we confined water molecules between two atomistically smooth graphite slabs. The simulation box was periodic in the x- and y-directions, while the z-direction, normal to the flow, was fixed and

https://doi.org/10.1017/jfm.2026.11309 Published online by Cambridge University Press

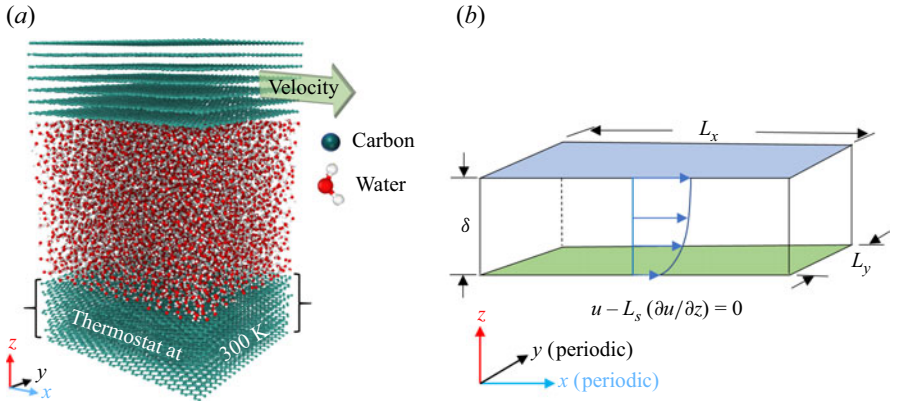


Figure 1. (*a*) Computational domain of an MD shear-driven flow model. (*b*) Computational domain for DNS with shear-dependent L_s.

non-periodic. In this fixed boundary condition, atoms were not allowed to move across or interact with the opposite side of the simulation box along the z-direction. The outermost graphene layers were excluded from time integration to maintain a constant channel height throughout the simulation.

The carbon atoms in the graphene sheets were modelled with a Tersoff (Lindsay & Broido 2010) force field, and the weak non-bonded graphene interlayer interactions were modelled with a Lennard-Jones (LJ) (Lindsay, Broido & Mingo 2011) force field. The LJ force field, commonly used to model non-bonded interactions, is expressed as

$$V(r) = 4\epsilon\left(\frac{\sigma^{12}}{r^{12}} - \frac{\sigma^{6}}{r^{6}}\right), \tag{2.1}$$

where V is the pairwise interaction energy as a function of the interatomic separation r, ϵ defines the depth of the potential well (energy scale), and σ represents the finite distance at which the potential energy becomes zero (length scale). In our simulations, graphite was selected as the wall material due to its broadly characterised interactions with water. The simulation domain consisted of graphite slabs measuring 62 Å × 54 Å in the $x-y$ plane, with thickness 20 Å. A total of 5491 water molecules occupied the gap between these solid surfaces, and the extended simple point charge model (SPC/E) in Ryckaert, Ciccotti & Berendsen (1977) and Ciccotti & Ryckaert (1986) was used to model its molecular interactions. The initial separation between the confining surfaces was approximately 50 Å. This distance was slightly adjusted to ensure that the bulk region of water, located sufficiently far from the solid–liquid interfaces, attained density $1.00 \pm 0.02\ \mathrm{g\,cm^{-3}}$ at 300 K. Upon reaching the target density, the system was deemed to have achieved a compressibility-free state at the corresponding temperature and density; see figure 2(*a*). Three distinct solid–liquid interactions were studied, corresponding to varying degrees of surface wettability and interfacial affinity. The interfacial interactions were modelled using the LJ potential. Traditionally, cross-interaction parameters in LJ models are determined using the Lorentz–Berthelot mixing rules (Lorentz 1881), where the energy scale is defined as the geometric mean $\epsilon_{ij} = (\epsilon_{ii}\epsilon_{jj})^{1/2}$, and the length scale as the arithmetic mean $\sigma_{ij} = (\sigma_{ii} + \sigma_{jj})/2$, of the LJ parameters optimised for the individual interface components. Although widespread in the literature, this practice has been deemed inadequate (Thompson & Troian 1997; Voronov *et al.* 2006, 2007; Petravic & Harrowell 2007). Alternatively, the solid–liquid LJ parameters can be optimised by

https://doi.org/10.1017/jfm.2026.11309 Published online by Cambridge University Press

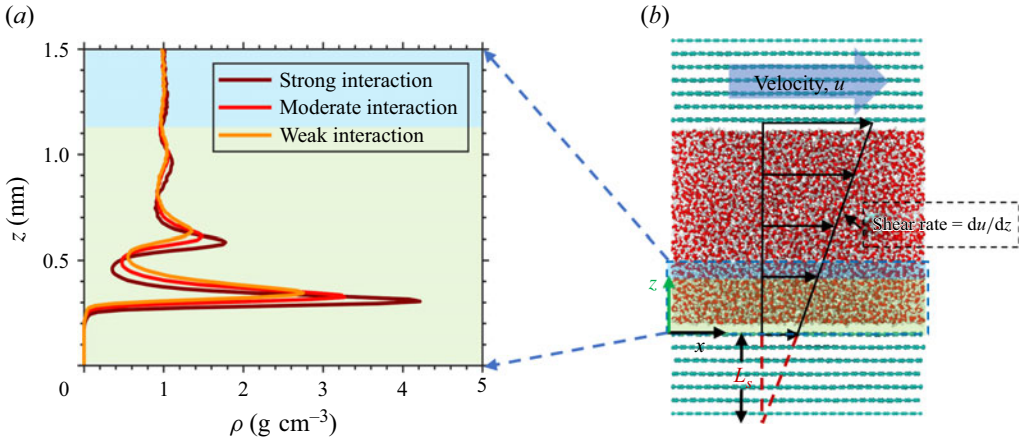


Figure 2. (*a*) Water density profiles for the difference interfacial models. (*b*) Schematic of the velocity profile in Couette flow. The shear rate is calculated from the slope of the velocity profile $\mathrm{d}u/\mathrm{d}z$.

fitting adsorption energy profiles obtained from first principles data such as Møller–Plesset perturbation theory of the second order (MP2) (Wu & Aluru 2013), density functional theory with symmetry-adapted perturbation theory (DFT–SAPT) (Jenness, Karalti & Jordan 2010), the random phase approximation (Ma *et al.* 2011), or coupled-cluster calculations with single and double excitations and perturbative triples (CCSD(T)) (Voloshina *et al.* 2011). In this study, three distinct solid–liquid interfaces were considered, corresponding to strong, moderate and weak interaction strengths. The LJ parameters for the strong interaction case were optimised by Wu & Aluru (2013) using CCSD(T)-based adsorption energy data, where both C–O and C–H interactions were parametrised by fitting to a single adsorption curve. The parameters for the moderate interaction case were adopted from Ramos-Alvarado (2019), who optimised C–O and C–H LJ parameters by fitting two adsorption curves obtained from random phase approximation data reported by Ma *et al.* (2011). Furthermore, the LJ parameters for the weak interaction case (C–O only) were obtained from Paniagua-Guerra *et al.* (2020), who employed the wettability–binding energy relationship proposed by Ramos-Alvarado (2019). This relationship provides an analytical connection between the LJ parameters and the equilibrium contact angle, verified through MD simulations, where the LJ parameters serve as input, and a size-independent contact angle emerges as the output. The corresponding LJ parameters for the three interface models are summarised in table 1. The resulting interfaces exhibited contact angles ranging from fully wetting (0°) to partially hydrophilic (64.4°).

In MD shear-driven flow, we applied shear by translating the top wall with a constant velocity ranging from 0.8 to 6 $\text{Å}\,\text{ps}^{-1}$, while keeping the bottom wall stationary. This approach for shear-driven flow in MD was adopted in previous literature (Thompson & Troian 1997; Voronov *et al.* 2006, 2007; Ho *et al.* 2011). The resulting shear rate in our simulation for each interfacial model was determined from the slope of the steady-state velocity profile, as illustrated in figure 2(*b*). Accordingly, the shear rate ($\dot{\gamma}_f$) in the NEMD simulations varied between 0.001 and 0.04 ps^{-1}.

Previous studies (Kannam *et al.* 2011, 2012; Ramos-Alvarado *et al.* 2016) have also reported that in the low-shear regime, L_s values obtained from NEMD simulations are consistent with those computed using equilibrium molecular dynamic (EMD), where the interfacial friction coefficient is evaluated through Green–Kubo relations derived from fluctuation–dissipation theory. In our simulations, we observe a similar level of

https://doi.org/10.1017/jfm.2026.11309 Published online by Cambridge University Press

Case ID	Reference	ϵ_{CO} (kJ mol^{-1})	σ (Å)	ϵ_{CH} (kJ mol^{-1})	σ (Å)	θ (deg.)
Weak interaction	Paniagua-Guerra *et al.* (2020)	0.3889	3.480	–	–	64.4
Moderate interaction	Ramos-Alvarado (2019)	0.3268	3.389	0.2033	2.647	48.4
Strong interaction	Wu & Aluru (2013), Voloshina *et al.* (2011)	0.6887	3.126	2.447	1.372	Film (0)

Table 1. The LJ parameters used for the interface models. The weak interaction includes only C–O interactions, while the moderate and strong interactions incorporate both C–O and C–H interactions.

consistency: the slip lengths obtained at low shear rates agree closely with the EMD results reported by Paniagua-Guerra *et al.* (2020), as shown in supplementary figure S1.

As MD simulations of flow require relatively high shear rates to produce noise-free data to bypass the short length scale and time scale compared to experimental conditions, the elevated shear rates induce significant viscous heating within the fluid, necessitating a means of thermal regulation. Several thermostating strategies exist, including applying a thermostat to all atoms (Thompson & Robbins 1990; Khare, Keblinski & Yethiraj 2006; Voronov *et al.* 2006), only to fluid atoms (Voronov *et al.* 2007; Thomas & McGaughey 2008; Zhang, Zhang & Ye 2009), or only to solid atoms (Nagayama & Cheng 2004; Martini *et al.* 2008*a*; Hansen, Todd & Daivis 2011; Kannam *et al.* 2011, 2012; Yong & Zhang 2013). Thermostating of the fluid atoms interrupts the natural flow dynamics by rescaling the velocity of the fluid particles, resulting in unphysical flow conditions (see Yong & Zhang 2013). In contrast, thermostating the solid wall provides a more physically consistent approach by mimicking heat transfer through a conductive boundary. In our simulations, a Nosè–Hoover (Hoover 1985) thermostat with time constant 0.1 ps was applied to the bottom graphite wall and maintained at 300 K to dissipate the excess heat generated by shear. The top wall was adiabatic, ensuring that heat was removed solely through the bottom surface, mimicking natural cooling.

The MD simulations were carried out in two stages: EMD and NEMD. In the EMD stage, the system was first equilibrated at 300 K for 1000 ps using the canonical ensemble (NVT), followed by an additional 1000 ps under the microcanonical ensemble (NVE) to verify the system's stability without external thermal control. In the NEMD stage, shear was applied by translating the top wall at a constant velocity. Each simulation was first run for 2000 ps to reach a statistically steady state, followed by a 5000 ps production run for data collection, with sampling performed every 0.5 ps. During NEMD simulations, the water molecules were integrated using pure Newtonian dynamics (no thermostat). The time step for the simulations was 0.001 ps.

2.2. *The DNS set-up*

The computational domain for DNS is a half-channel configuration, as illustrated in figure 1(*b*). The coordinate system is defined with x, y and z representing the streamwise, spanwise and wall-normal directions, respectively. Periodic boundary conditions are applied in the streamwise and spanwise directions. A stress-free boundary condition, defined as $\partial u/\partial z = \partial v/\partial z = 0$ and $w = 0$, was applied at the top boundary, while an MD-informed shear-dependent slip condition was used at the bottom wall. In our DNS framework, a constant streamwise pressure gradient $\mathrm{d}p/\mathrm{d}x = 1$ was applied. The mean wall shear stress was therefore $\tau_m = 1$ due to force balance. Accordingly, the friction velocity was 1 in all DNS. A detailed formulation and discussion of the shear-dependent slip condition is presented in § 4.

https://doi.org/10.1017/jfm.2026.11309 Published online by Cambridge University Press

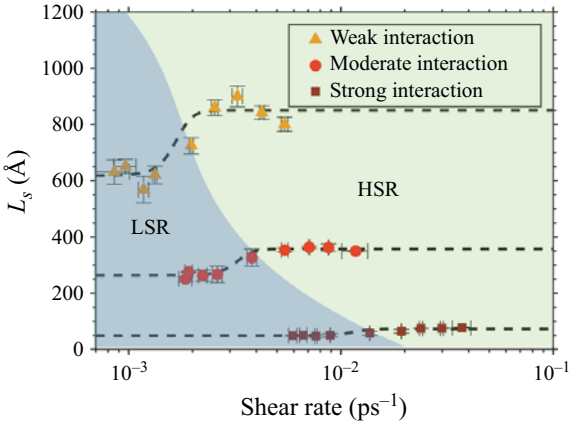


Figure 3. The MD results, showing the slip length L_s as a function of shear rate. The boundary between the two shaded regions represents the critical shear rate. The dashed lines are the sigmoid fittings. The fitted parameters are listed in table 2.

The computational domain spans $L_x = 8\pi\delta$ in the streamwise direction and $L_y = 3\pi\delta$ in the spanwise direction (where $\delta = 1$ is the channel half-height); the wall-normal extent is δ. Uniform grid spacing is employed in the homogeneous directions, with $\Delta x^+ \approx 12$ and $\Delta y^+ \approx 6$. The solver is pseudo-spectral in the streamwise and spanwise directions, for which grids slightly coarser than the conventional $\Delta x^+ \approx 10$ and $\Delta y^+ \approx 5$ are generally adequate (Bernardini, Pirozzoli & Orlandi 2014; Oliver *et al.* 2014; Thompson *et al.* 2016; Chen *et al.* 2022).

The wall-normal resolution is determined following the recommendations of Yang & Griffin (2021) and Pirozzoli & Orlandi (2021). Accordingly, a non-uniform mesh is adopted to resolve the wall unit in the viscous sublayer, and the local Kolmogorov length scale in the logarithmic and outer regions. The minimum and maximum wall-normal spacings are $\Delta z^+_{min} \approx 0.34$ and $\Delta z^+_{max} \approx 3.73$ for $Re_\tau = 180$, $\Delta z^+_{min} \approx 0.47$ and $\Delta z^+_{max} \approx 5.17$ for $Re_\tau = 400$, and $\Delta z^+_{min} \approx 0.59$ and $\Delta z^+_{max} \approx 6.47$ for $Re_\tau = 1000$, ensuring adequate near-wall resolution without over-resolving the channel core. The sampling duration in each case satisfies the heuristic requirement of approximately $10\delta/u_\tau$ (Pirozzoli, Bernardini & Orlandi 2016), ensuring statistical convergence of the first- and second-order turbulence statistics. To validate our DNS code, simulations with constant $L_s = 0.02\delta$ were performed, matching the configuration of Min & Kim (2004). Very good agreement was observed between the present results and those of Min & Kim (2004), as shown in supplementary figure S2.

The DNS are performed using LESGO, an open-source parallel pseudo-spectral large-eddy simulation code. It solves the filtered Navier–Stokes equations using pseudo-spectral discretisation in the streamwise and spanwise directions, and a second-order finite-difference scheme in the wall-normal direction. The LESGO code, along with its modified implementations, has been extensively utilised in numerous investigations of turbulent channel flows, as evidenced by prior studies (see Bou-Zeid, Meneveau & Parlange 2005; Anderson & Meneveau 2011; Abkar & Porté-Agel 2012; Zhu *et al.* 2017; Yang *et al.* 2019).

3. The MD results

Figure 3 illustrates the variation of L_s as a function of the shear stress for different interface affinity levels. We see that in all cases, L_s exhibits a bimodal dependence on shear, characterised by two distinct regimes: a low-shear regime (LSR) and a high-shear regime (HSR),

https://doi.org/10.1017/jfm.2026.11309 Published online by Cambridge University Press

Case ID	$\dot{\gamma}_c$ (ps^{-1})	$\dot{\gamma}_t$ (ps^{-1})	R^2
Weak interaction	0.0017	1.61×10^{-4}	0.83
Moderate interaction	0.0032	2.97×10^{-4}	0.95
Strong interaction	0.0113	1.20×10^{-3}	0.79

Table 2. Fitted parameters ($\dot{\gamma}_c$ and $\dot{\gamma}_t$) for the sigmoid function describing the shear-dependent slip length (L_s) obtained from MD simulations. Here, $\dot{\gamma}_c$ represents the critical shear rate marking the transition from the LSR to HSR, and $\dot{\gamma}_t$ characterises the sharpness of the transition.

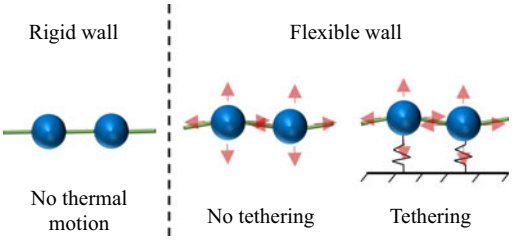


Figure 4. Schematic of rigid and flexible walls in MD simulations.

separated by a sharp transition. Furthermore, this bimodal behaviour can be captured by a sigmoid function. Accordingly, L_s values for different interface models were fitted using the sigmoid expression $L_s = (L_{HSR} - L_{LSR})/(1 + \exp[-(\dot{\gamma}_f - \dot{\gamma}_c)/\dot{\gamma}_t]) + L_{LSR}$, where $\dot{\gamma}_c$ and $\dot{\gamma}_t$ are fitting parameters. Here, $\dot{\gamma}_c$ represents the transition point from LSR to HSR, and $\dot{\gamma}_t$ determines the sharpness of the transition. The MD data showed good agreement with the sigmoid fits, as indicated by the dashed lines in figure 3. The corresponding R^2 values for the weak, moderate and strong interaction cases were 0.83, 0.95 and 0.79, respectively. The fitted parameters are listed in table 2. This motivates the development of a phenomenological model for the DNS study, which is discussed in § 4.

Note that previous studies have reported contrasting trends in the shear dependence of L_s. Thompson & Troian (1997), Kannam *et al.* (2011, 2012) and Wagemann *et al.* (2017) reported an unbounded growth of L_s with increasing shear rates. This unbounded growth of L_s with shear can be attributed to the use of rigid/fixed wall atoms in earlier studies, which suppressed momentum transfer between the wall and liquid atoms. This was verified in Martini *et al.* (2008*a*), who conducted simulations with both fixed- and flexible-wall atoms. Their results showed that rigid walls led to an unbounded growth of L_s at high shear rates, while flexible walls produced a bounded growth of L_s.

Figure 4 schematically illustrates the different wall conditions used in MD simulations. In the rigid- or fixed-wall configuration, the solid atoms are excluded from time integration, ensuring that their positions remain immobile throughout the simulation (left-hand panel). This approach is computationally cheap but neglects atomic vibrations and consequently the exchange of energy and momentum between the solid and the fluid (see Martini *et al.* 2008*a*). At finite temperatures, however, solid atoms possess non-zero kinetic energy and vibrate around their equilibrium positions (middle panel). These thermal vibrations are essential for maintaining thermodynamic consistency, as they enable realistic coupling between the wall and the fluid. To prevent unphysical centre-of-mass drift of the solid wall – while still retaining natural thermal motion – an invisible tether was applied to each solid atom (right-hand panel). This tethering technique acts as an elastic spring that anchors atoms to their equilibrium lattice positions without freezing

https://doi.org/10.1017/jfm.2026.11309 Published online by Cambridge University Press

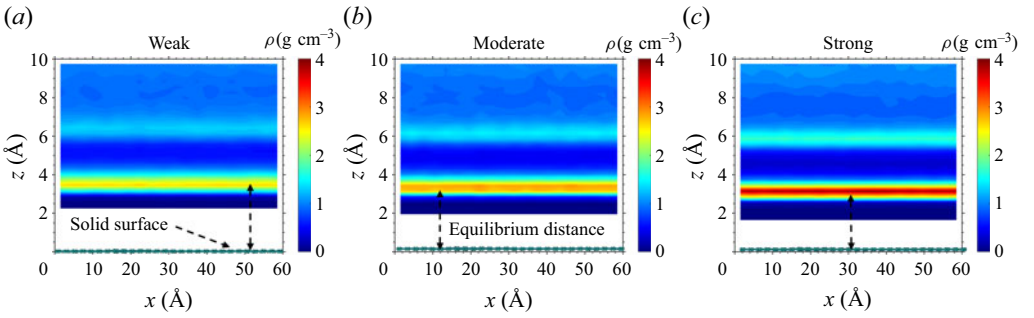


Figure 5. Density contours of water in (*a*) weak interaction, (*b*) moderate interaction, (*c*) strong interaction. The white gap is the complete repulsion region.

them. The tether constrains translational motion of the solid but allows atoms to vibrate freely within the potential well defined by the spring, thereby preserving the thermal motion and realistic energy exchange characteristic of a flexible-wall model. In our shear-driven flow simulations, the bottom solid wall was tethered to prevent unwanted drift arising from the high shear rates applied to the top wall.

The bimodal behaviour of L_s with respect to shear has been interpreted through several theoretical frameworks. Martini *et al.* (2008*b*) employed the variable-density Frenkel–Kontorova model (Lichter, Roxin & Mandre 2004). At low shear rates, they identified a defect slip, where liquid molecules transition discretely by jumping from one equilibrium site to another. As the shear rate increases, this localised hopping mechanism gives way to a global slip in which the entire liquid layer moves collectively. Similarly, Babu & Sathian (2012) described shear-dependent L_s behaviour based on transition-state theory. They suggested that liquid molecules need to overcome an activation energy barrier to jump from one equilibrium position to another. The transition from the LSR to the HSR occurs when the applied shear stress overcomes the activation energy for momentum transfer. An experimental study by Li *et al.* (2014) provided additional support for the LSR-to-HSR transition. In their investigation of Poiseuille flow in silicon nanochannels, they observed a sharp increase in L_s when the applied pressure gradient matched the adhesive forces between the liquid and the wall. Beyond this threshold, further increases in shear rate resulted in a plateau in the measured L_s. More recently, Shuvo *et al.* (2024*b*) explored the rheology of water and the friction coefficient at the interface to understand the bimodal response of L_s. They indicate that while both the viscosity and the friction coefficient remain approximately constant at low shear, they decrease at higher shear rates. Notably, the friction coefficient declined more rapidly than the viscosity during the transition, resulting in an effective increase in slip length. In the HSR, the system reached a new steady state in which L_s became approximately constant.

The LSR-to-HSR transition observed in our MD simulations occurs at different shear rates depending on the solid–liquid affinity strength, as shown in figure 3. The critical shear rate increases with increasing solid–liquid affinity. This shift can be attributed to two key interfacial properties: the equilibrium distance between liquid molecules and the solid wall, and the local concentration of liquid particles at the interface. Figure 5 illustrates the density contours of water near the solid surface for different interfacial affinities. It is observed that a stronger solid–liquid affinity results in a smaller solid–liquid equilibrium distance, as indicated by the small gap between the wall and the highest density layer. Additionally, stronger solid–liquid interactions yield a higher molecular concentration at the interface. The peak densities for the weak, moderate and strong interaction cases were

https://doi.org/10.1017/jfm.2026.11309 Published online by Cambridge University Press

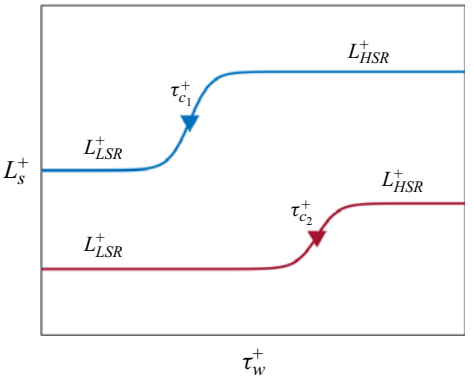


Figure 6. Schematic representation of MD-informed shear-dependent L_s used in the DNS solver.

approximately 2.67, 2.81 and 3.75 g cm^{-3}, respectively (see figure 5). These observations suggest that as the interfacial interaction strengthens, the liquid molecules become more tightly bound to the wall, both spatially and structurally. Consequently, a higher shear stress is required to induce the transition to the HSR. Thus the increase in critical shear rate with increasing solid–liquid affinity arises from the combined effects of reduced equilibrium distance and the concentration of liquid molecules at the interface.

4. Shear-dependent slip boundary condition for DNS

The MD results presented in § 3 show a shear-dependent and bimodal slip behaviour, characterised by a transition from LSR to HSR. Based on this finding, we develop a shear-dependent slip boundary condition for use in DNS of turbulent channel flow. To incorporate the MD-informed slip dynamics into the continuum model, a phenomenological model is constructed in the form of a sigmoid function. This model captures the transition between LSR and HSR by smoothly varying L_s^+ as a function of wall shear stress τ_w^+:

$$L_s^+ = \frac{L^+_{HSR} - L^+_{LSR}}{1 + \exp\left(-\dfrac{\tau_w^+ - \tau_c^+}{b}\right)} + L^+_{LSR}, \tag{4.1}$$

where L^+_{HSR} and L^+_{LSR} denote the slip lengths at HSR and LSR, respectively, and τ_c^+ is the critical wall shear stress. The parameter b determines the steepness of the transition between LSR and HSR, with its value $b = 0.05$ based on MD simulations.

The critical shear stress τ_c^+ reflects the solid–liquid interaction, where a higher τ_c^+ corresponds to stronger solid–liquid affinity. Figure 6 illustrates the L_s^+–shear stress relationship, showing the transition from the low plateau (L^+_{LSR}) to the high plateau (L^+_{HSR}). For this study, five critical wall shear stress values ($\tau_c^+ = 0.8, 0.9, 1.0, 1.1, 1.2$) were considered. Figure 7 compares the instantaneous slip length distributions for three representative cases: no-slip (see figure 7*a*), shear-dependent L_s (see figure 7*b*), and constant slip length (see figure 7*c*). Unlike the constant-slip case, the stress-dependent model produces a bimodal slip length distribution, shifting between L_{LSR} and L_{HSR} as the local wall shear stress fluctuates across the critical value τ_c. This introduces a dynamic coupling absent in constant-slip models: the activation of slip is intermittent and governed by the proximity of the instantaneous wall shear stress to the critical stress, $|\tau_w - \tau_c|$.

https://doi.org/10.1017/jfm.2026.11309 Published online by Cambridge University Press

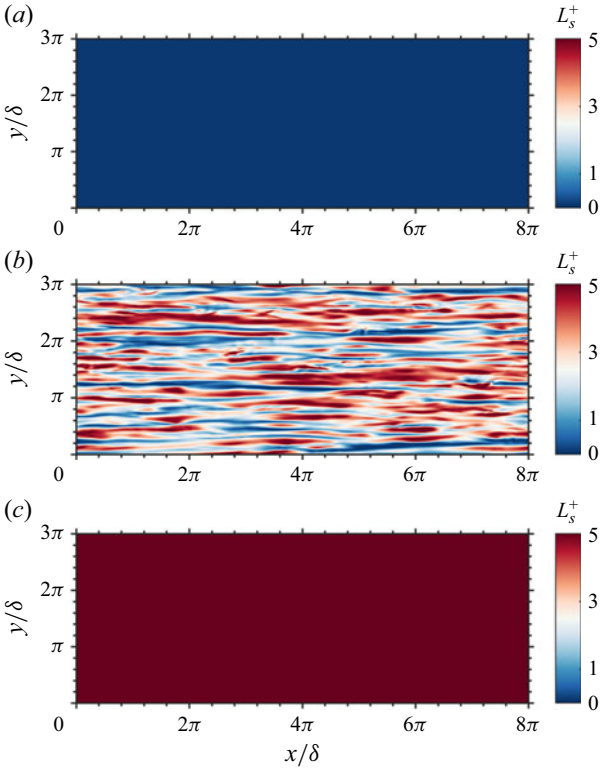


Figure 7. Contours of slip length employed in DNS for (*a*) no-slip ($L_s^+ = 0$), (*b*) shear-dependent slip (Re180T3 in table 3), and (*c*) constant slip ($L_s^+ = 5$).

To ensure that L_s values used in the DNS were comparable to previous works, we selected $L_{LSR}^+ = 0.1$ and $L_{HSR}^+ = 5$ for the shear-dependent cases. Shuvo *et al.* (2024*b*) reported that the L_{HSR}/L_{LSR} ratio remains constant and independent of the solid–liquid affinity. Thus the values of L_{LSR}^+ and L_{HSR}^+ were kept fixed in all shear-dependent L_s cases in the DNS study. The MD results show that the transitions from L_{LSR} to L_{HSR} vary for different interface models, resulting in distinct critical shear rates for each interface model (see figure 3). To account for these effects in DNS, τ_c^+ in the sigmoid function was varied, while the values of L_{LSR}^+ and L_{HSR}^+ remained fixed. In this study, the slip boundary condition was applied only in the streamwise direction. A summary of the simulation parameters is provided in table 3.

Finally, we note that in the present DNS, slip is applied exclusively to the streamwise velocity component, with impermeability and no-slip imposed on the wall-normal and spanwise components. This specification is not an arbitrary modelling choice; rather, it is a direct consequence of the MD-derived constitutive law and the stress levels characteristic of the flow. The MD results indicate that the interface transitions from a low-slip to a slip regime only when the local wall shear stress exceeds a critical threshold τ_c. In the present configuration, the mean spanwise velocity is zero; lacking a mean shear component, the instantaneous spanwise wall shear stress $\tau_{w,z}$ remains well below τ_c for the range of affinities considered here. Under the stress-conditioned law, the spanwise direction therefore remains effectively in a low-to-no-slip regime. Consequently, imposing $w = 0$ at the wall is a physical implication of the stress-conditioned framework rather than a discretionary modelling simplification.

https://doi.org/10.1017/jfm.2026.11309 Published online by Cambridge University Press

Case ID	$Re_\tau = u_\tau \delta / \nu$	L_x/δ	L_y/δ	N_x	N_y	N_z	L^+_{HSR}	L^+_{LSR}	τ_c^+
Re180NS	180	8π	3π	378	284	80	0	0	NA
Re180T1	180	8π	3π	378	284	80	5	0.1	0.8
Re180T2	180	8π	3π	378	284	80	5	0.1	0.9
Re180T3	180	8π	3π	378	284	80	5	0.1	1.0
Re180T4	180	8π	3π	378	284	80	5	0.1	1.1
Re180T5	180	8π	3π	378	284	80	5	0.1	1.2
Re180CS	180	8π	3π	378	284	80	5	5	NA
Re400NS	400	8π	3π	838	628	128	0	0	NA
Re400T1	400	8π	3π	838	628	128	5	0.1	0.8
Re400T2	400	8π	3π	838	628	128	5	0.1	0.9
Re400T3	400	8π	3π	838	628	128	5	0.1	1.0
Re400T4	400	8π	3π	838	628	128	5	0.1	1.1
Re400T5	400	8π	3π	838	628	128	5	0.1	1.2
Re400CS	400	8π	3π	838	628	128	5	5	NA
Re1000T3	1000	8π	3π	1950	1400	257	5	0.1	1.0
Re1000CS	1000	8π	3π	1950	1400	257	5	5	NA

Table 3. DNS details. For cases where $L^+_{HSR} = L^+_{LSR}$, a uniform slip length is employed therefore τ_c^+ is not needed. Here, NS stands for no slip, CS stands for constant slip, and T1 to T5 represent various critical τ_c^+ values. The Re1000NS data (no-slip, $Re_\tau = 1000$) are from Lee & Moser (2015).

5. The DNS results

We investigate the impact of a shear-dependent slip on the near-wall dynamics in a turbulent plane channel flow.

5.1. *Mean flow*

Figures 8(*a–c*) depict the mean streamwise velocity profiles normalised by the friction velocity $U^+ = \langle u \rangle / u_\tau$ for $Re_\tau = 180$, 400, 1000. For the no-slip cases (NS), the velocity profile conforms to the classical structure of wall-bounded turbulence, showing a linear variation in the viscous sublayer ($z^+ < 5$), and a logarithmic distribution in the log-law region ($z^+ > 30$). The introduction of hydrodynamic slip in the streamwise direction, whether constant (CS) or shear-dependent (T1–T5), does not significantly alter the shape of the velocity profiles; see figures 8(*d–f*). However, an upward shift is observed in both the constant and shear-dependent L_s cases, reflecting the reduced drag facilitated by hydrodynamic slip.

The T1–T5 cases exhibit a systematic variation in the velocity profiles with respect to the critical wall shear stress parameter τ_c, in a manner consistent with our MD analysis. In the MD analysis, the transition from LSR to HSR depends on solid–liquid interactions, and the critical shear is highest for the most hydrophilic case. Consistently, the DNS cases with the weakest solid–liquid affinity ($\tau_c^+ = 0.8$, T1) exhibit the highest slip velocity at the wall, while the cases with the strongest affinity ($\tau_c^+ = 1.2$, T5) show the lowest slip velocity at the wall. This trend is further supported by the statistical behaviour of L_s, as shown in figure 9(*a*). We see that the mean L_s decreases monotonically with increasing τ_c^+, reflecting the growing dominance of the LSR in the flow field. A somewhat interesting observation is the behaviour of the root mean square (RMS) of L_s. We see from figure 9(*b*) that it has a non-monotonic trend. The RMS of L_s is the highest for the T3 ($\tau_c^+ = 1$) cases, and the lowest for the T1 and T5 cases. We attribute this to the broad distribution of L_s in the T3 cases. Unlike T3, L_s is predominantly in the HSR and the LSR for T1

https://doi.org/10.1017/jfm.2026.11309 Published online by Cambridge University Press

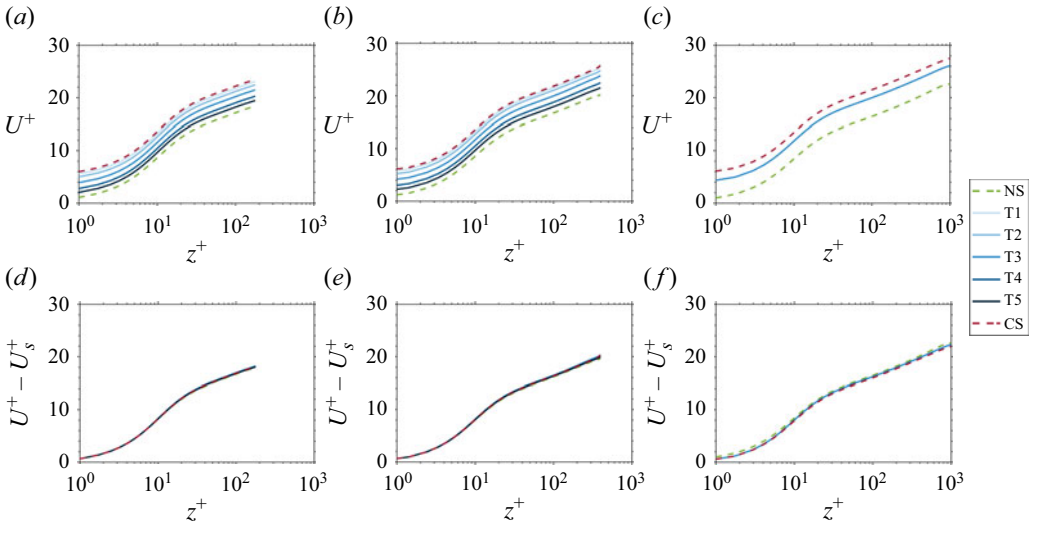


Figure 8. Mean streamwise velocity profiles ($U^+ = \langle u \rangle / u_\tau$) for (*a*) $Re_\tau = 180$, (*b*) $Re_\tau = 400$, (*c*) $Re_\tau = 1000$, and mean profiles $U^+ - U_s^+$ for (*d*) $Re_\tau = 180$, (*e*) $Re_\tau = 400$, (*f*) $Re_\tau = 1000$.

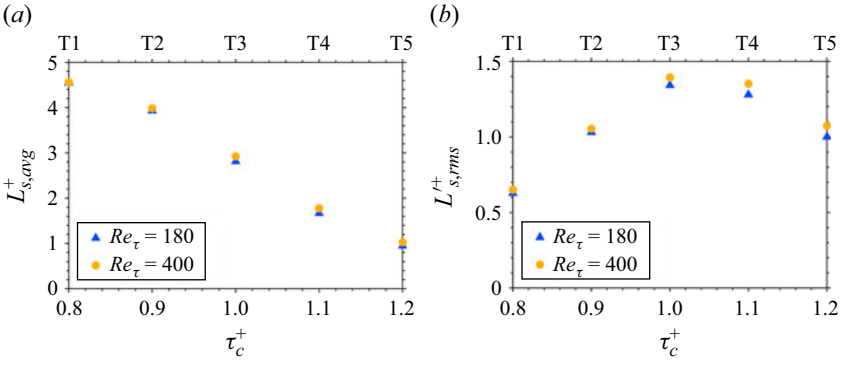


Figure 9. (*a*) Mean slip length as a function of solid–liquid affinity. (*b*) Slip length RMS as a function of solid–liquid affinity.

and T5, respectively. Furthermore, in the limiting cases where $\tau_c^+ \ll \tau_w$ or $\tau_c^+ \gg \tau_w$, the instantaneous wall shear stress rarely crosses the transition threshold. As a result, L_s remains effectively confined to the HSR or the LSR, respectively. In these limits, L_s becomes essentially constant in time, and its fluctuations vanish, leading to a near-zero RMS value. This behaviour corresponds to the effective constant-slip limit.

5.2. *Turbulence intensity*

In this subsection, we report on the effect of a shear-dependent L_s on turbulence intensity. Figure 10 illustrates $\langle u'u' \rangle$, $\langle v'v' \rangle$, $\langle w'w' \rangle$ for all cases for $Re_\tau = 180$, 400 and 1000. The wall-normal and spanwise velocity variances are not notably affected by the streamwise slip. The streamwise turbulence variance $\langle u'u' \rangle$ shows an upward shift for CS and T1–T5 cases compared to the NS cases near the wall, indicating increased turbulence intensity near the wall; see figures 10(*a–c*). In contrast to the mean flow results, where the T1–T5 cases are bounded by the NS and CS cases, the T1–T5 results here lie outside the bounds

https://doi.org/10.1017/jfm.2026.11309 Published online by Cambridge University Press

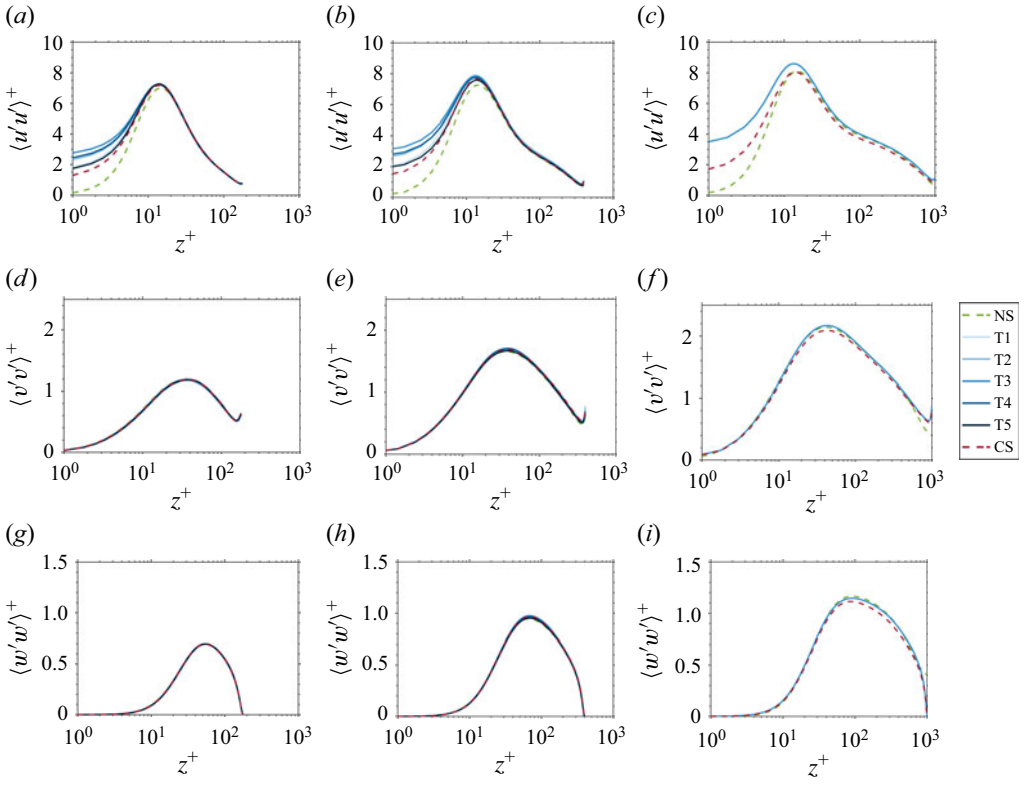


Figure 10. Reynolds stress: (*a*) $\langle u'u' \rangle^+$ at $Re_\tau = 180$, (*b*) $\langle u'u' \rangle^+$ at $Re_\tau = 400$, (*c*) $\langle u'u' \rangle^+$ at $Re_\tau = 1000$, (*d*) $\langle v'v' \rangle^+$ at $Re_\tau = 180$, (*e*) $\langle v'v' \rangle^+$ at $Re_\tau = 400$, (*f*) $\langle v'v' \rangle^+$ at $Re_\tau = 1000$, (*g*) $\langle w'w' \rangle^+$ at $Re_\tau = 180$, (*h*) $\langle w'w' \rangle^+$ at $Re_\tau = 400$, (*i*) $\langle w'w' \rangle^+$ at $Re_\tau = 1000$.

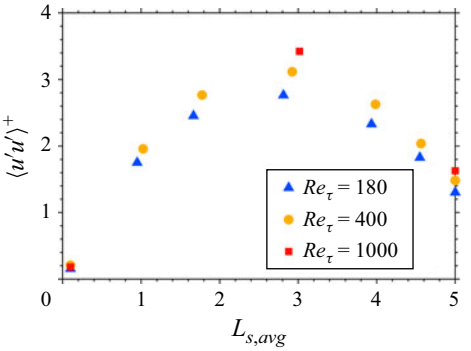


Figure 11. Plot of $\langle u'u' \rangle^+$ as a function of $L_{s,avg}$ at $z^+ \approx 1$.

defined by the NS and CS cases. This result suggests that compared to a constant L_s, shear-dependent L_s leads to different turbulence dynamics near the wall.

Among the cases with a shear-dependent L_s, the near-wall turbulence intensity does not vary monotonically with drag reduction. Instead, as shown in figure 11, the streamwise intensity attains a maximum in case T3, then decreases. This non-monotonic trend indicates that the mean slip length alone is insufficient to parametrise the near-wall turbulence response. The physical mechanism is illustrated in figure 12, which plots the amplification

https://doi.org/10.1017/jfm.2026.11309 Published online by Cambridge University Press

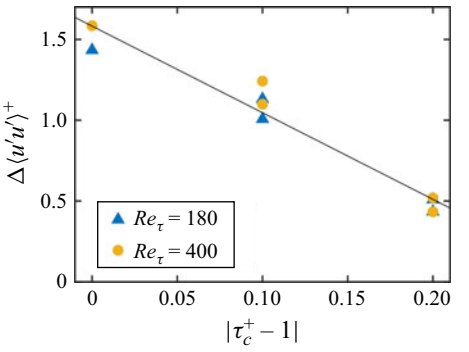


Figure 12. Amplification of $\Delta\langle u'u'\rangle^+$ at $z^+ = 1$, relative to the constant-slip baseline, plotted as a function of the proximity of the mean wall shear stress to the critical stress, $|\tau_c - \langle\tau_w\rangle|^+$. The thin solid line is a linear fit of the data.

of streamwise intensity $\Delta\langle u'u'\rangle^+$ against the proximity of the mean wall shear stress to the critical stress, $|\tau_c - \langle\tau_w\rangle|^+$. Peak amplification occurs when the mean stress lies close to the slip-activation threshold ($\langle\tau_w\rangle \approx \tau_c$). In this regime, instantaneous wall shear stress fluctuations frequently cross τ_c, so the boundary condition switches intermittently between the low- and high-slip branches. This threshold-crossing intermittency introduces strong, stress-correlated perturbations in the wall layer, and maximises $\Delta\langle u'u'\rangle^+$. When $\langle\tau_w\rangle$ is far from τ_c – either well below the threshold (effectively no-slip) or well above it (slip-saturated) – the switching is rare and the near-wall intensity approaches the constant-slip baseline. Finally, we observe a Reynolds number effect consistent with canonical wall-bounded flows: increasing Reynolds number increases near-wall turbulence intensity (Marusic *et al.* 2013), superposed on the slip-induced effects described above.

5.3. *Energy spectra*

It is clear from $\langle u'u'\rangle$ that the near-wall turbulence does not solely depend on the mean of L_s, and shear-dependent L_s significantly affects the near-wall turbulence. In this subsection, we investigate the impact from the perspective of the energy spectra. Here, considering that we did not see a significant impact of the streamwise shear-dependent L_s on the spanwise and wall-normal turbulence intensities, we focus on the streamwise velocity. Figure 13 and supplementary figure S3 present the pre-multiplied energy spectra of streamwise velocity fluctuations for $Re_\tau = 180$ and 400, respectively. The spectra highlight the energy contributions of different streamwise length scales ($\lambda_x = 2\pi/k_x$) across the wall-normal distance. In figure 13 and supplementary figure S3, the contour plots reveal that the inner energy peak, associated with near-wall turbulence, remains fixed at $z^+ \approx 15$, and $\lambda_x^+ = \lambda_x u_\tau/\nu \approx 1000$ for all cases. While the slip boundary condition does not alter the inner peak location, it leads to noticeable changes in the magnitude and distribution of streamwise near-wall energy. Both CS and T1–T5 cases exhibit an overall intensification of streamwise near-wall energy. Specifically, the spectra for T1–T5 cases exhibit slightly wider energy contours near the wall, which is attributed to enhanced intermittency in L_s.

It is clear from the pre-multiplied energy spectra that shear-dependent L_s affects the viscous sublayer the most. Here, we focus on $k_x E_{uu}(z^+ = 1)$ as a function of the streamwise wavelength; see figure 14. Similar to the Reynolds stress results, the spectra for the T1–T5 cases are not bounded by the NS and CS cases. For the NS case, there is not much energy in the streamwise velocity at $z^+ = 1$. In contrast, the CS and T1–T5

https://doi.org/10.1017/jfm.2026.11309 Published online by Cambridge University Press

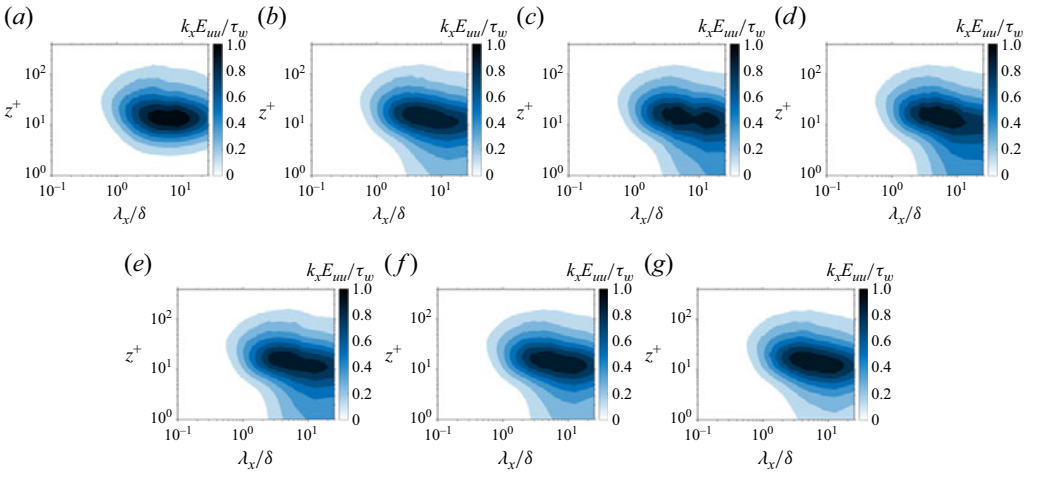


Figure 13. Pre-multiplied energy spectra of streamwise velocity with respect to wall normal direction for (*a*) Re180NS, (*b*) Re180T1, (*c*) Re180T2, (*d*) Re180T3, (*e*) Re180T4, (*f*) Re180T5, (*g*) Re180CS.

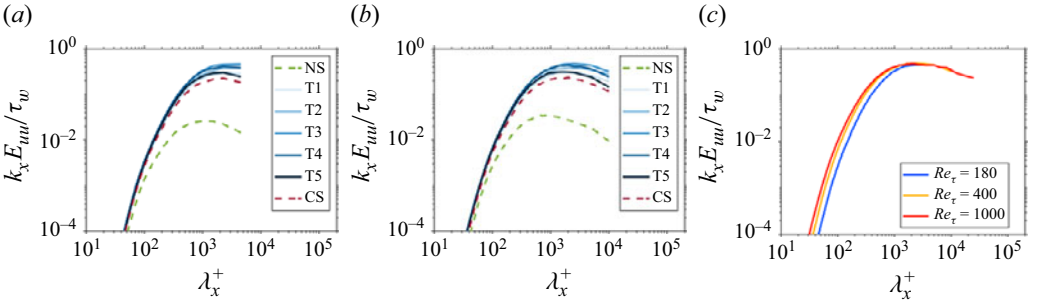


Figure 14. Variation of pre-multiplied energy spectra of streamwise velocity with λ_x^+ at $z^+ \approx 1$ for (*a*) $Re_\tau = 180$, (*b*) $Re_\tau = 400$, (*c*) different Re_τ for $\tau_c^+ = 1$ (T3 case).

cases exhibit enhanced energy across a wider range of wavelengths. While the T1–T5 spectra agree with the CS spectrum in the short-wavelength region ($\lambda_x^+ < 1000$), they exhibit peak shifts towards longer wavelengths. This trend suggests that the presence of shear-dependent L_s affects the large scales more than the small scales. Figure 14(*c*) compares the near-wall spectra at $z^+ = 1$ for three Reynolds numbers ($Re_\tau = 180$, 400 and 1000) under the same parametrisation of the interfacial interaction ($\tau_c^+ = 1$). We observe that increasing the Reynolds number increases the small-scale spectral energy content, consistent with known finite-Reynolds-number effects (Wei & Willmarth 1989).

5.4. *Near-wall motions*

In the previous subsections, we found that the shear-dependent L_s substantially modifies the viscous sublayer dynamics, and affects the large scales more than the small scales. Here, we further examine the spatial organisation of the streamwise velocity fluctuations.

To characterise large-scale motions in turbulent channel flow, Yoon *et al.* (2016) applied a two-dimensional Gaussian filter with cut-off wavelength 1δ, and reported streamwise elongation of structures up to 20δ under constant-slip boundary conditions. Motivated by their approach, we apply a Fourier spectral filter in the streamwise direction with cut-off wavelength 3δ to separate large-scale motions from smaller near-wall structures.

https://doi.org/10.1017/jfm.2026.11309 Published online by Cambridge University Press

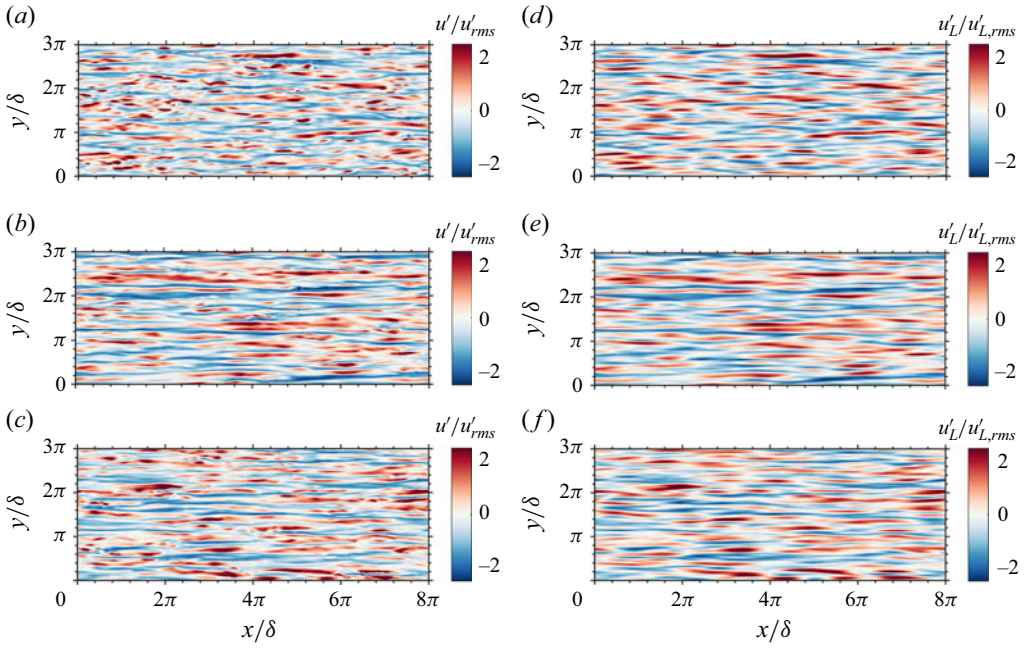


Figure 15. Unfiltered instantaneous flow field for (*a*) Re180NS, (*b*) Re180T3, (*c*) Re180CS; and filtered flow field for (*d*) Re180NS, (*e*) Re180T3, (*f*) Re180CS. Supplementary figure S4 presents the unfiltered and filtered flow field for all cases with $Re_\tau = 180$.

Any separation of the streamwise spectra into 'small' and 'large' scales depends on the choice of cut-off and is not unique. The results below should therefore be interpreted relative to this specific cut-off. Figure 15 shows instantaneous streamwise velocity fields at $z^+ \approx 3$ together with the corresponding filtered fields. The filtered fields reveal elongated near-wall streaks under shear-slip-dependent L_s conditions, although this qualitative view alone does not establish whether the large scales are more energetic.

To quantify how different scales contribute to the streamwise turbulence intensity, we decompose the streamwise fluctuation into a large-scale component u'_L and a small-scale component u'_{sm} obtained from the spectral filter. The streamwise intensity can then be written as

$$\langle u'u' \rangle^+ = \langle u'_L u'_L \rangle^+ + \langle u'_{sm} u'_{sm} \rangle^+ + 2\langle u'_L u'_{sm} \rangle^+. \tag{5.1}$$

Figures 16(*a–c*) show this decomposition for $Re_\tau = 180$, 400 and 1000. For a fixed Reynolds number, the small-scale contribution is similar across T1–T5, whereas the large-scale contribution varies appreciably among these cases. This supports the conclusion that shear-dependent L_s primarily modifies the large-scale component of the near-wall streamwise intensity, consistent with the trends discussed in figure 14. By contrast, increasing Reynolds number primarily increases the small-scale energy content, and the presence of shear-dependent L_s does not qualitatively alter this known Reynolds number trend.

5.5. *Turbulent kinetic energy budget*

To find what physical process is responsible for the enhanced turbulence in the wall layer, we analyse the turbulent kinetic energy (TKE) budget with a focus on the viscous sublayer ($z^+ \lesssim 5$). The TKE per unit mass is defined as $k = (1/2)\langle u'_i u'_i \rangle$, and its budget equation is

https://doi.org/10.1017/jfm.2026.11309 Published online by Cambridge University Press

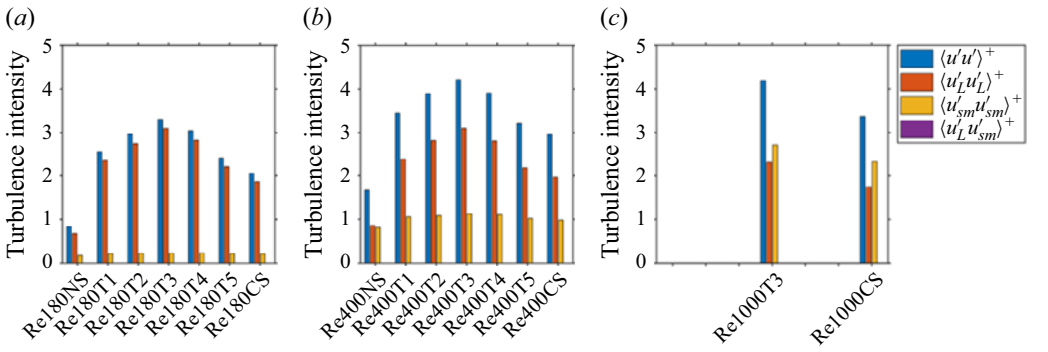


Figure 16. Streamwise turbulence intensity decomposition in large- and small-scale structures at (*a*) $Re_\tau = 180$, (*b*) $Re_\tau = 400$, and (*c*) $Re_\tau = 1000$.

expressed as

$$\frac{\mathrm{D}k}{\mathrm{D}t} = 0 = -\underbrace{\frac{1}{\rho}\frac{\partial \langle p' u_i' \rangle}{\partial x_i}}_{\text{pressure diffusion, } \Pi} - \underbrace{\frac{1}{2}\frac{\partial \langle u_j' u_j' u_i' \rangle}{\partial x_i}}_{\text{turbulent transport, } T} - \underbrace{\langle u_i' u_j' \rangle \frac{\partial \langle u_i \rangle}{\partial x_j}}_{\text{production, } P} + \underbrace{\nu \frac{\partial^2 k}{\partial x_i^2}}_{\text{molecular viscous transport, } D} - \underbrace{\nu \left\langle \frac{\partial u_i'}{\partial x_j} \frac{\partial u_i'}{\partial x_j} \right\rangle}_{\text{dissipation, } \epsilon}. \tag{5.2}$$

Figure 17 illustrates the constituent terms of the TKE budget for both $Re_\tau = 180$ and $Re_\tau = 400$. Beyond the viscous layer ($z^+ > 5$), all terms appear to be largely invariant under slip conditions. However, significant differences emerge within the viscous sublayer, especially in the dissipation and viscous diffusion terms. Figure 18 further illustrates the terms in the TKE equation at $z^+ \approx 1$. The dissipation rate ϵ is markedly reduced in the T1–T5 cases, with the lowest dissipation observed in case T3. As τ_c^+ deviates from 1, the dissipation increases symmetrically: T1 and T5 exhibit the highest dissipation among the shear-dependent configurations, while T2 and T4 show intermediate levels. As the dissipation in the viscous sublayer is balanced by the viscous diffusion, a similar trend is observed in the viscous diffusion term (D), which varies as the dissipation varies. This result suggests that it is the reduced dissipation that leads to the increased turbulence in the shear-dependent slip boundary condition.

6. A model for the mean flow

In this section, we develop a model for the mean velocity profile in turbulent channel flow with shear-dependent slip boundary conditions.

6.1. *The mean momentum equation and the mixing-length closure*

For fully developed turbulent channel flow, the mean momentum equation reads

$$\nu \frac{\partial^2 \langle u \rangle}{\partial z^2} + \frac{\partial \left(-\langle u'w' \rangle \right)}{\partial z} - \frac{1}{\rho}\frac{\mathrm{d}P}{\mathrm{d}x} = 0, \tag{6.1}$$

where $-\langle u'w' \rangle$ is the Reynolds shear stress and is the only unclosed term. We introduce an eddy viscosity ν_t and close the Reynolds shear stress as

$$-\langle u'w' \rangle = \nu_t \frac{\partial \langle u \rangle}{\partial z}. \tag{6.2}$$

https://doi.org/10.1017/jfm.2026.11309 Published online by Cambridge University Press

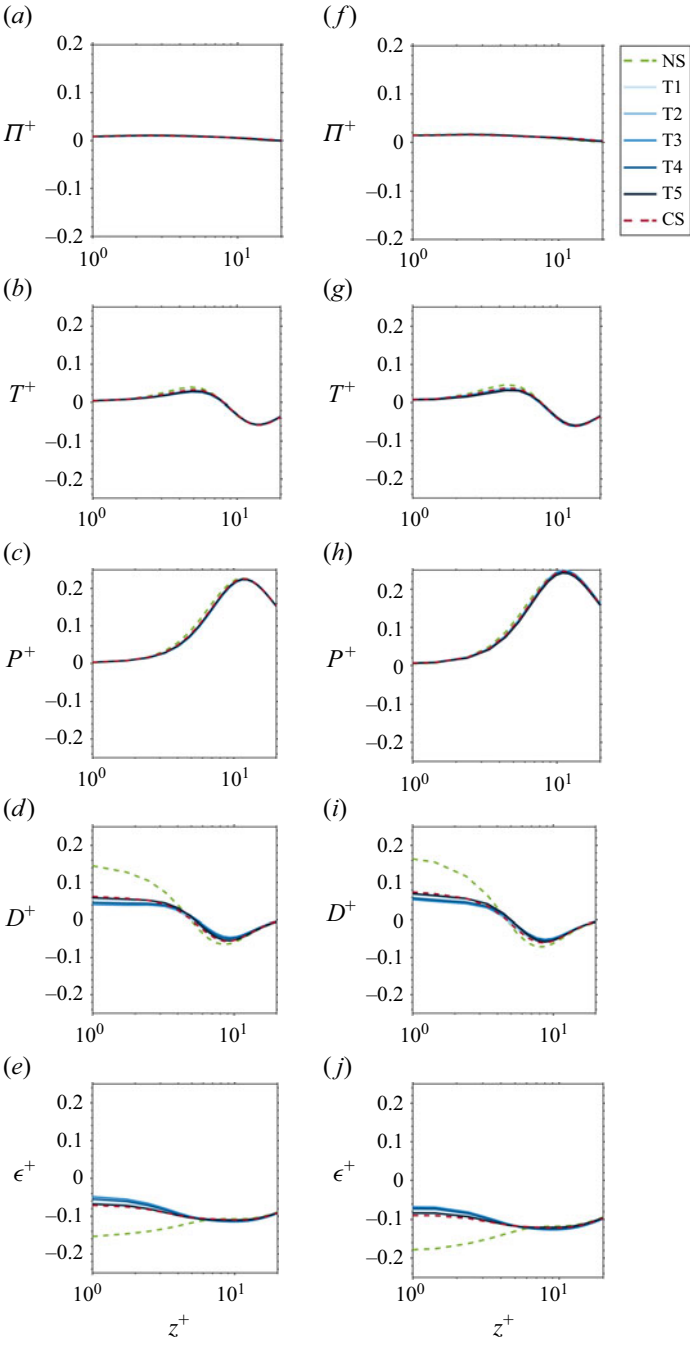


Figure 17. The TKE budget terms for $Re_\tau = 180$ (*a*) pressure diffusion Π^+, (*b*) turbulent transport T^+, (*c*) production P^+, (*d*) molecular viscous transport D^+, (*e*) dissipation ϵ^+; and TKE terms for $Re_\tau = 400$ (*f*) pressure diffusion Π^+, (*g*) turbulent transport T^+, (*h*) production P^+, (*i*) molecular viscous transport D^+, (*j*) dissipation ϵ^+.

https://doi.org/10.1017/jfm.2026.11309 Published online by Cambridge University Press

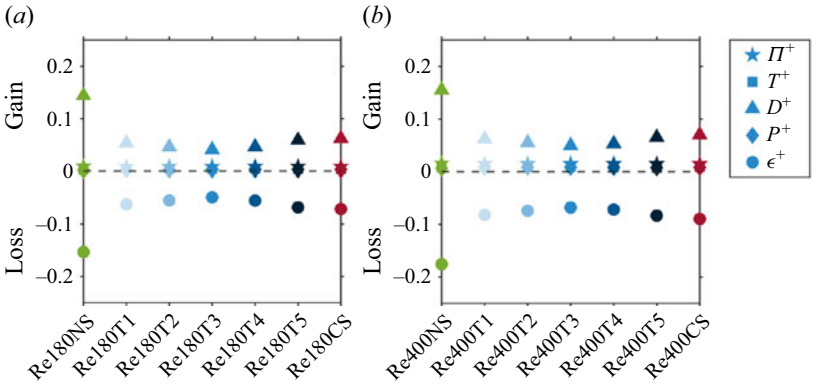


Figure 18. The TKE terms at $z^+ \approx 1$ for (*a*) $Re_\tau = 180$, (*b*) $Re_\tau = 400$.

We model ν_t using Prandtl's mixing-length hypothesis (Prandtl 1925):

$$\nu_t = l^2 \left| \frac{\partial \langle u \rangle}{\partial z} \right|, \tag{6.3}$$

where l is the mixing length. Following Yang *et al.* (2024), we set

$$l = \min\left[l_{IL},\ l_{OL}\right], \tag{6.4}$$

with the inner-layer mixing length

$$l_{IL} = \kappa z D, \tag{6.5}$$

where $\kappa = 0.4$ is the von Kármán constant, and D is a van-Driest-type damping function (van Driest 1956):

$$D = 1 - \exp(-z^+/A^+_{VD}), \tag{6.6}$$

with $A^+_{VD} = 26$. The outer-layer mixing length is taken as $l_{OL} = 0.085\delta$ (Kays, Crawford & Weigand 2005).

6.2. *Modelling the slip velocity*

To predict the mean flow, we also require the mean slip velocity at the wall. Since slip depends on L_s, and L_s depends on the wall shear stress, we first model the wall shear stress statistics. The probability density functions (PDFs) of wall shear stress are skewed (figure 19). When the critical shear stress is smaller than the mean wall shear stress (e.g. T1 and T2), the PDFs exhibit positive skewness; when $\tau_c > \tau_m$ (e.g. T4 and T5), they exhibit negative skewness. The variation of the skewness of wall shear stress across all cases is presented in supplementary figure S5. To capture this behaviour, we model the PDFs using a skew-normal distribution with

$$\mathrm{PDF}(\tau_w) = \frac{2}{\omega\sqrt{2\pi}} \exp\left[-\frac{(\tau_w - \tau_\xi)^2}{2\omega^2}\right] \int_{-\infty}^{\alpha(\tau_w - \tau_\xi)/\omega} \frac{1}{\sqrt{2\pi}} \exp\left(-\frac{t^2}{2}\right) \mathrm{d}t, \tag{6.7}$$

where τ_ξ, ω and α control the location, scale and shape, respectively. The location parameter is related to the mean τ_m as

$$\tau_\xi = \tau_m - \omega\delta_1\sqrt{\frac{2}{\pi}}, \tag{6.8}$$

https://doi.org/10.1017/jfm.2026.11309 Published online by Cambridge University Press

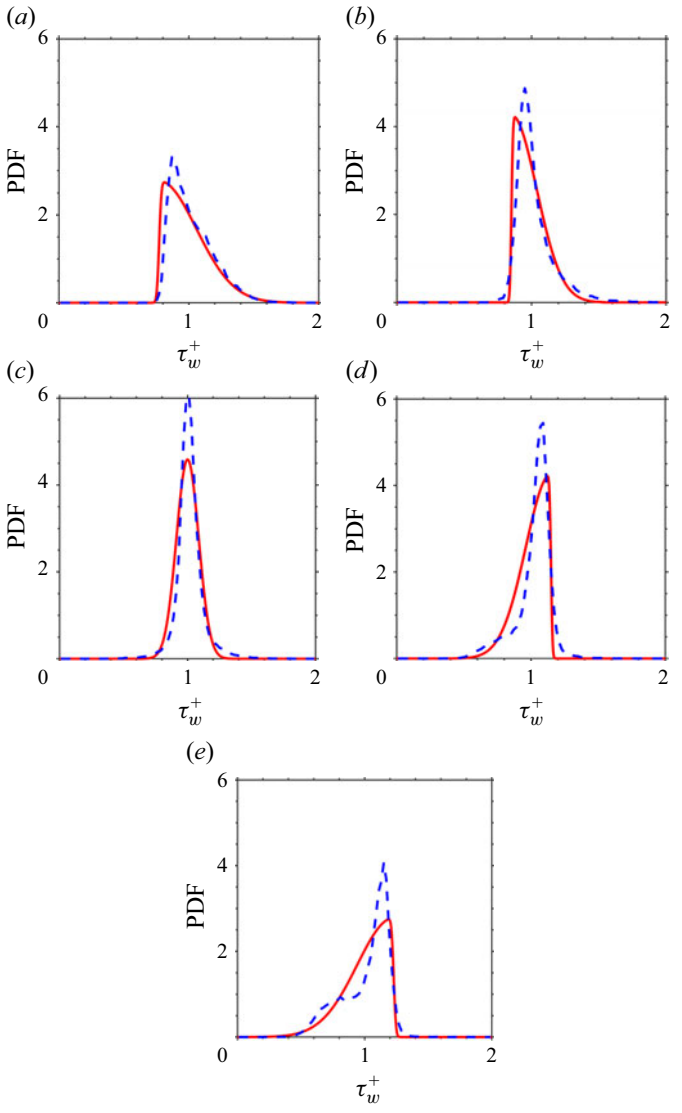


Figure 19. The PDFs of wall shear stress for (*a*) Re180T1, (*b*) Re180T2, (*c*) Re180T3, (*d*) Re180T4, (*e*) Re180T5. The solid red lines denote a skew-normal distribution, and the dashed blue lines are the PDFs obtained from DNS.

with $\delta_1 = \alpha/\sqrt{1+\alpha^2}$.

A closed-form relation expressing α directly in terms of skewness is not available in general, except for the special case $\alpha = 0$, which corresponds to the standard normal distribution. In the present work, we set $\alpha = 20$ for $\Delta\tau^+ = \tau_c^+ - \tau_m^+ > 0$, and $\alpha = -20$ for $\Delta\tau^+ < 0$, so that $|\delta_1|$ approaches its maximal attainable value ($\delta_1 \approx \pm 1$). Positive δ_1 corresponds to a right-skewed distribution, while negative δ_1 produces a left-skewed distribution. The maximum theoretical skewness of a skew-normal distribution is obtained in the limit $\delta_1 \to \pm 1$. Accordingly, the skewness in our model is given by

$$\gamma_1 = \frac{4-\pi}{2}\frac{(\delta_1\sqrt{2/\pi})^3}{\left(1-2\delta_1^2/\pi\right)^2}, \quad \gamma_1 \in [-1, 1]. \tag{6.9}$$

https://doi.org/10.1017/jfm.2026.11309 Published online by Cambridge University Press

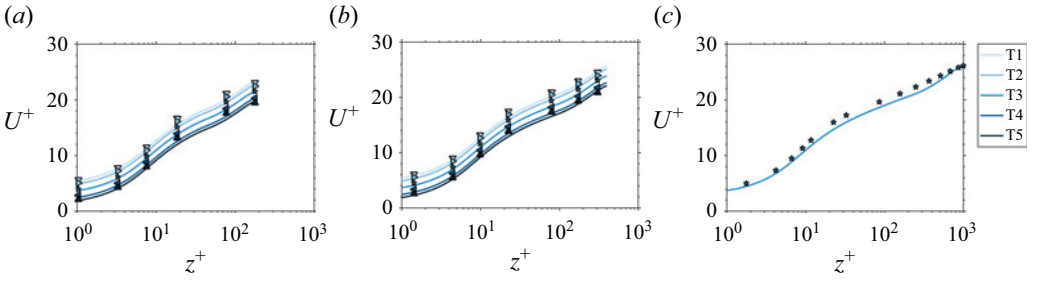


Figure 20. Mean velocity profiles $U^+ = \langle u \rangle / u_\tau$ using our model analysis at (*a*) $Re_\tau = 180$, (*b*) $Re_\tau = 400$, (*c*) $Re_\tau = 1000$. The markers in the velocity profiles denote DNS data.

The scale parameter ω, which controls the spread of the distribution, is modelled as

$$\omega = |\Delta\tau^+| + c, \tag{6.10}$$

where $c = 0.087$ is a model parameter. This constant is introduced to capture the finite variance of the wall shear stress fluctuations observed in the DNS data, and was determined by fitting the model variance to the DNS results. Figures 19(*a–e*) compare the modelled PDFs with the DNS data.

With a model for PDF(τ_w), we estimate the mean slip velocity at the wall. The instantaneous slip velocity is

$$u_{z=0} = L_s \frac{\partial u}{\partial z} = \frac{1}{\nu} L_s \tau_w = \frac{1}{\nu}(L_s + L_s')(\tau_w + \tau_w'). \tag{6.11}$$

Taking the average yields

$$\langle u \rangle_{z=0} = \frac{1}{\nu}\left(\langle L_s \rangle \langle \tau_w \rangle + \langle L_s' \tau_w' \rangle\right), \tag{6.12}$$

where $\langle L_s' \tau_w' \rangle$ is the covariance between L_s and τ_w. Under the stress-conditioned relation $L_s = L_s(\tau_w)$, it can be evaluated from the modelled PDF as

$$\langle L_s' \tau_w' \rangle = \int_{-\infty}^{\infty} L_s' \tau_w' \, \mathrm{PDF}(\tau_w) \, \mathrm{d}\tau_w. \tag{6.13}$$

6.3. *Results*

The model predictions follow directly from the formulation above. For each case, the parameters δ, u_τ, ν, τ_m, τ_c, L_{LSR} and L_{HSR} are taken from the corresponding DNS to enable a one-to-one comparison. These inputs define the modelled wall shear stress distribution, and through $L_s(\tau_w)$, the corresponding mean slip condition at the wall. Figure 20 compares the resulting mean velocity profiles with the DNS data. Across $Re_\tau = 180$, 400 and 1000, the model shows good agreement with the DNS, and captures the overall mean flow behaviour.

7. Conclusions

This study integrates nanoscale insights from MD simulations with continuum-scale DNS to investigate turbulent channel flows with shear-dependent interfacial slip. The MD results show that the slip length is well described by a threshold-like constitutive relation: it remains approximately constant in low-slip and high-slip regimes, with a sharp transition near a critical wall shear stress that varies systematically with solid–liquid

https://doi.org/10.1017/jfm.2026.11309 Published online by Cambridge University Press

affinity. Guided by this constitutive behaviour, we impose a local, stress-conditioned slip boundary condition in DNS at $Re_\tau = 180$, 400 and 1000. The DNS results show that the logarithmic region is largely preserved, aside from an approximately constant upward shift, and the mean velocity profiles remain bounded between the no-slip and constant-slip limits. Consistent with this, the mean response (mean drag/mean shift) is governed primarily by the mean level of slip implied by the constitutive relation. In contrast, the near-wall turbulence response cannot be parametrised by the mean slip alone. The streamwise Reynolds stress in the viscous sublayer exhibits a non-monotonic dependence on the slip-activation threshold: amplification is strongest when the mean wall shear stress lies close to the critical stress, and it weakens as the mean stress moves away from the threshold. This behaviour is consistent with threshold-crossing intermittency: when the instantaneous wall shear stress fluctuates across the critical value, the boundary condition switches intermittently between low- and high-slip branches, introducing strong stress-correlated perturbations in the near-wall region. Spectral filtering and spectra further indicate that the changes in streamwise intensity are carried predominantly by the large-scale component under the present cut-off, while the Reynolds number effect primarily increases small-scale energy as in canonical channel flows. The TKE budget analysis suggests that reduced viscous dissipation is a key contributor to the observed structural changes. Finally, we propose a mixing-length model that incorporates a skew-normal representation of the wall shear stress distribution together with the stress-conditioned slip law to predict the mean velocity profile, and the model shows good agreement with the DNS mean profiles. Overall, this work provides a multiscale framework that links interfacial molecular physics to continuum-scale wall-bounded turbulence, and highlights the central role of stress-conditioned slip – and its activation relative to wall-stress statistics – in controlling near-wall turbulence over drag-altering materials.

Supplementary material. Supplementary material is available at https://doi.org/10.1017/jfm.2026.11309.

Funding. This research is supported by the National Science Foundation, USA (award no. 2241730).

Declaration of interests. The authors report no conflict of interest.

AI assistance statement. An AI-based language tool was used for minor language editing (grammar and clarity). All content was reviewed and verified by the authors.

References

ABKAR, M. & PORTÉ-AGEL, F. 2012 A new boundary condition for large-eddy simulation of boundary-layer flow over surface roughness transitions. *J. Turbul.* **13**, N23.

ALIZADEH PAHLAVAN, A. & FREUND, J.B. 2011 Effect of solid properties on slip at a fluid–solid interface. *Phys. Rev. E* **83** (2), 021602.

ANDERSON, W. & MENEVEAU, C. 2011 Dynamic roughness model for large-eddy simulation of turbulent flow over multiscale, fractal-like rough surfaces. *J. Fluid Mech.* **679**, 288–314.

BABU, J.S. & SATHIAN, S.P. 2012 Combining molecular dynamics simulation and transition state theory to evaluate solid–liquid interfacial friction in carbon nanotube membranes. *Phys. Rev. E* **85** (5), 051205.

BERNARDINI, M., PIROZZOLI, S. & ORLANDI, P. 2014 Velocity statistics in turbulent channel flow up to $Re_\tau = 4000$.
J. Fluid Mech. **742**, 171–191.

BOU-ZEID, E., MENEVEAU, C. & PARLANGE, M. 2005 A scale-dependent Lagrangian dynamic model for large eddy simulation of complex turbulent flows. *Phys. Fluids* **17** (2), 025105.

BUSSE, A. & SANDHAM, N.D. 2012 Influence of an anisotropic slip-length boundary condition on turbulent channel flow. *Phys. Fluids* **24** (5), 055111.

CHEN, P.E.S., LV, Y., XU, H.H.A., SHI, Y. & YANG, X.I.A. 2022 LES wall modeling for heat transfer at high speeds. *Phys. Rev. Fluids* **7** (1), 014608.

CHEN, Y., LI, D., JIANG, K., YANG, J., WANG, X. & WANG, Y. 2006 Hydrodynamic lubrication in nanoscale bearings under high shear velocity. *J. Chem. Phys.* **125** (8), 084702.

https://doi.org/10.1017/jfm.2026.11309 Published online by Cambridge University Press

CHOI, C.-H., WESTIN, K.J.A. & BREUER, K.S. 2003 Apparent slip flows in hydrophilic and hydrophobic microchannels. *Phys. Fluids* **15** (10), 2897–2902.

CICCOTTI, G. & RYCKAERT, J.-P. 1986 Molecular dynamics simulation of rigid molecules. *Comput. Phys. Rep.* **4** (6), 345–392.

CRAIG, V.S.J., NETO, C. & WILLIAMS, D.R.M. 2001 Shear-dependent boundary slip in an aqueous Newtonian liquid. *Phys. Rev. Lett.* **87** (5), 054504.

FRENKEL, D. & SMIT, B. 2023 *Understanding Molecular Simulation: From Algorithms to Applications*, 3rd edn. Elsevier.

HANSEN, J.S., TODD, B.D. & DAIVIS, P.J. 2011 Prediction of fluid velocity slip at solid surfaces. *Phys. Rev. E* **84** (1), 016313.

HO, T.A., PAPAVASSILIOU, D.V., LEE, L.L. & STRIOLO, A. 2011 Liquid water can slip on a hydrophilic surface. *Proc. Natl Acad. Sci. USA* **108** (39), 16170–16175.

HOOVER, W.G. 1985 Canonical dynamics: equilibrium phase-space distributions. *Phys. Rev. A* **31** (3), 1695–1697.

IBRAHIM, J.I., GÓMEZ-DE-SEGURA, G., CHUNG, D. & GARCÍA-MAYORAL, R. 2021 The smooth-wall-like behaviour of turbulence over drag-altering surfaces: a unifying virtual-origin framework. *J. Fluid Mech.* **915**, A56.

JENNESS, G.R., KARALTI, O. & JORDAN, K.D. 2010 Benchmark calculations of water–acene interaction energies: extrapolation to the water–graphene limit and assessment of dispersion-corrected DFT methods. *Phys. Chem. Chem. Phys.* **12** (24), 6375–6381.

KANNAM, S.K., TODD, B.D., HANSEN, J.S. & DAIVIS, P.J. 2011 Slip flow in graphene nanochannels. *J. Chem. Phys.* **135** (14), 144701.

KANNAM, S.K., TODD, B.D., HANSEN, J.S. & DAIVIS, P.J. 2012 Slip length of water on graphene: limitations of non-equilibrium molecular dynamics simulations. *J. Chem. Phys.* **136** (2), 024705.

KAYS, W.M., CRAWFORD, M.E. & WEIGAND, B. 2005 *Convective Heat and Mass Transfer*, 4th edn. McGraw-Hill.

KHARE, R., KEBLINSKI, P. & YETHIRAJ, A. 2006 Molecular dynamics simulations of heat and momentum transfer at a solid–fluid interface: relationship between thermal and velocity slip. *Intl J. Heat Mass Transfer* **49** (19–20), 3401–3407.

LEE, M. & MOSER, R.D. 2015 Direct numerical simulation of turbulent channel flow up to $Re_\tau = 5200$. *J. Fluid Mech.* **774**, 395–415.

LI, L., MO, J. & LI, Z. 2014 Flow and slip transition in nanochannels. *Phys. Rev. E* **90** (3), 033003.

LICHTER, S., ROXIN, A. & MANDRE, S. 2004 Mechanisms for liquid slip at solid surfaces. *Phys. Rev. Lett.* **93** (8), 086001.

LINDSAY, L. & BROIDO, D.A. 2010 Optimized Tersoff and Brenner empirical potential parameters for lattice dynamics and phonon thermal transport in carbon nanotubes and graphene. *Phys. Rev. B* **81** (20), 205441.

LINDSAY, L., BROIDO, D.A. & MINGO, N. 2011 Flexural phonons and thermal transport in multilayer graphene and graphite. *Phys. Rev. B* **83** (23), 235428.

LORENTZ, H.A. 1881 Ueber die anwendung des satzes vom virial in der kinetischen theorie der gase. *Ann. Phys.* **248** (1), 127–136.

MA, J., MICHAELIDES, A., ALFE, D., SCHIMKA, L., KRESSE, G. & WANG, E. 2011 Adsorption and diffusion of water on graphene from first principles. *Phys. Rev. B* **84** (3), 033402.

MARTINI, A., HSU, H.-Y., PATANKAR, N.A. & LICHTER, S. 2008*a* Slip at high shear rates. *Phys. Rev. Lett.* **100** (20), 206001.

MARTINI, A., ROXIN, A., SNURR, R.Q., WANG, Q. & LICHTER, S. 2008*b* Molecular mechanisms of liquid slip. *J. Fluid Mech.* **600**, 257–269.

MARUSIC, I., MONTY, J.P., HULTMARK, M. & SMITS, A.J. 2013 On the logarithmic region in wall turbulence. *J. Fluid Mech.* **716**, R3.

MIN, T. & KIM, J. 2004 Effects of hydrophobic surface on skin-friction drag. *Phys. Fluids* **16** (7), L55–L58.

NAGAYAMA, G. & CHENG, P. 2004 Effects of interface wettability on microscale flow by molecular dynamics simulation. *Intl J. Heat Mass Transfer* **47** (3), 501–513.

OLIVER, T.A., MALAYA, N., ULERICH, R. & MOSER, R.D. 2014 Estimating uncertainties in statistics computed from direct numerical simulation. *Phys. Fluids* **26** (3), 035101.

PANIAGUA-GUERRA, L.E., GONZALEZ-VALLE, C.U. & RAMOS-ALVARADO, B. 2020 Effects of the interfacial modeling approach on equilibrium calculations of slip length for nanoconfined water in carbon slits. *Langmuir* **36** (48), 14772–14781.

PARK, H., PARK, H. & KIM, J. 2013 A numerical study of the effects of superhydrophobic surface on skin-friction drag in turbulent channel flow. *Phys. Fluids* **25** (11), 110815.

https://doi.org/10.1017/jfm.2026.11309 Published online by Cambridge University Press

PETRAVIC, J. & HARROWELL, P. 2007 On the equilibrium calculation of the friction coefficient for liquid slip against a wall. *J. Chem. Phys.* **127** (17), 174706.

PIROZZOLI, S., BERNARDINI, M. & ORLANDI, P. 2016 Passive scalars in turbulent channel flow at high Reynolds number. *J. Fluid Mech.* **788**, 614–639.

PIROZZOLI, S. & ORLANDI, P. 2021 Natural grid stretching for DNS of wall-bounded flows. *J. Comput. Phys.* **439**, 110408.

PLIMPTON, S. 1995 Fast parallel algorithms for short-range molecular dynamics. *J. Comput. Phys.* **117** (1), 1–19.

PRANDTL, L. 1925 Bericht über untersuchungen zur ausgebildeten turbulenz. *Z. Angew. Appl. Maths Mech.* **5** (2), 136–139.

RAMOS-ALVARADO, B. 2019 Water wettability of graphene and graphite, optimization of solid–liquid interaction force fields, and insights from mean-field modeling. *J. Chem. Phys.* **151** (11), 114701.

RAMOS-ALVARADO, B., KUMAR, S. & PETERSON, G.P. 2016 Hydrodynamic slip length as a surface property. *Phys. Rev. E* **93** (2), 023101.

RAPAPORT, D.C. 2004 *The Art of Molecular Dynamics Simulation*, 2nd edn. Cambridge University Press.

RYCKAERT, J.-P., CICCOTTI, G. & BERENDSEN, H.J.C. 1977 Numerical integration of the Cartesian equations of motion of a system with constraints: molecular dynamics of *n*-alkanes. *J. Comput. Phys.* **23** (3), 327–341.

SHUVO, A.A., GONZALEZ-VALLE, C.U., YANG, X. & RAMOS-ALVARADO, B. 2024*a* Assessment of the free shear boundary condition in a capillary meniscus via molecular dynamics. *Phys. Fluids* **36** (11), 112031.

SHUVO, A.A., PANIAGUA-GUERRA, L.E., CHOI, J., KIM, S.H. & ALVARADO, B.R. 2025 Hydrodynamic slip in nanoconfined flows: a review of experimental, computational, and theoretical progress. *Nanoscale* **17**, 635–660.

SHUVO, A.A., PANIAGUA-GUERRA, L.E., YANG, X. & RAMOS-ALVARADO, B. 2024*b* Hydrodynamic slip characteristics of shear-driven water flow in nanoscale carbon slits. *J. Chem. Phys.* **160** (19), 194704.

STUKOWSKI, A. 2009 Visualization and analysis of atomistic simulation data with OVITO – the open visualization tool. *Model. Simul. Mater. Sci. Engng* **18** (1), 015012.

THOMAS, J.A. & MCGAUGHEY, A.J.H. 2008 Reassessing fast water transport through carbon nanotubes. *Nano Lett.* **8** (9), 2788–2793.

THOMPSON, P.A. & ROBBINS, M.O. 1990 Shear flow near solids: epitaxial order and flow boundary conditions. *Phys. Rev. A* **41** (12), 6830–6837.

THOMPSON, P.A. & TROIAN, S.M. 1997 A general boundary condition for liquid flow at solid surfaces. *Nature* **389** (6649), 360–362.

THOMPSON, R.L., SAMPAIO, L.E.B., DE BRAGANÇA, A., FELIPE, A.V., THAIS, L. & MOMPEAN, G. 2016 A methodology to evaluate statistical errors in DNS data of plane channel flows. *Comput. Fluids* **130**, 1–7.

VAN DRIEST, E.R. 1956 On turbulent flow near a wall. *J. Aeronaut. Sci.* **23** (11), 1007–1011.

VOLOSHINA, E., USVYAT, D., SCHÜTZ, M., DEDKOV, Y. & PAULUS, B. 2011 On the physisorption of water on graphene: a CCSD(T) study. *Phys. Chem. Chem. Phys.* **13** (25), 12041–12047.

VORONOV, R.S., PAPAVASSILIOU, D.V. & LEE, L.L. 2006 Boundary slip and wetting properties of interfaces: correlation of the contact angle with the slip length. *J. Chem. Phys.* **124** (20), 204701.

VORONOV, R.S., PAPAVASSILIOU, D.V. & LEE, L.L. 2007 Slip length and contact angle over hydrophobic surfaces. *Chem. Phys. Lett.* **441** (4–6), 273–276.

WAGEMANN, E., OYARZUA, E., WALTHER, J.H. & ZAMBRANO, H.A. 2017 Slip divergence of water flow in graphene nanochannels: the role of chirality. *Phys. Chem. Chem. Phys.* **19** (13), 8646–8652.

WEI, T. & WILLMARTH, W.W. 1989 Reynolds-number effects on the structure of a turbulent channel flow. *J. Fluid Mech.* **204**, 57–95.

WU, Y. & ALURU, N.R. 2013 Graphitic carbon–water nonbonded interaction parameters. *J. Phys. Chem. B* **117** (29), 8802–8813.

YANG, X.I.A., CHEN, P.E.S., ZHANG, W. & KUNZ, R. 2024 Predictive near-wall modelling for turbulent boundary layers with arbitrary pressure gradients. *J. Fluid Mech.* **993**, A1.

YANG, X.I.A., XU, H.H.A., HUANG, X.L.D. & GE, M.-W. 2019 Drag forces on sparsely packed cube arrays. *J. Fluid Mech.* **880**, 992–1019.

YANG, X.I.A. & GRIFFIN, K.P. 2021 Grid-point and time-step requirements for direct numerical simulation and large-eddy simulation. *Phys. Fluids* **33** (1), 015108.

YONG, X. & ZHANG, L.T. 2013 Thermostats and thermostat strategies for molecular dynamics simulations of nanofluidics. *J. Chem. Phys.* **138** (8), 084503.

YOON, M., HWANG, J., LEE, J., SUNG, H.J. & KIM, J. 2016 Large-scale motions in a turbulent channel flow with the slip boundary condition. *Intl J. Heat Fluid Flow* **61**, 96–107.

https://doi.org/10.1017/jfm.2026.11309 Published online by Cambridge University Press

ZHANG, Z.Q., ZHANG, H.W. & YE, H.F. 2009 Pressure-driven flow in parallel-plate nanochannels. *Appl. Phys. Lett.* **95** (15), 154101.

ZHU, X., IUNGO, G.V., LEONARDI, S. & ANDERSON, W. 2017 Parametric study of urban-like topographic statistical moments relevant to *a priori* modelling of bulk aerodynamic parameters. *Boundary-Layer Meteorol.* **162** (2), 231–253.

https://doi.org/10.1017/jfm.2026.11309 Published online by Cambridge University Press